

Coupling between elastic strain and interstitial fluid flow: Ramifications for poroelastic imaging

Ricardo Leiderman, Paul E. Barbone, Assad A. Oberai[‡],
and Jeffrey C. Bamber[§]

Department of Aerospace and Mechanical Engineering, Boston University,
Boston, MA 02215

E-mail: leider@bu.edu, barbone@bu.edu, oberaa@rpi.edu, jeff@icr.ac.uk

Abstract. We study the effects of interstitial fluid flow and interstitial fluid drainage on the spatio-temporal response of soft tissue strain. The motivation stems from the ability to measure *in vivo* strain distributions in soft tissue via elastography, and the desire to explore the possibility of using such techniques to investigate soft tissue fluid flow. Our study is based upon a mathematical model for soft tissue mechanics from the literature. It is a simple generalization of biphasic theory that includes coupling between the fluid and solid phases of the soft tissue, and crucially, fluid exchange between the interstitium and the local microvasculature. We solve the mathematical equations in two dimensions by the finite element method (FEM). The finite element implementation is validated against an exact analytical solution that is derived in the appendix. Realistic input tissue properties from the literature are used in conjunction with FEM modeling to conduct several computational experiments. The results of these lead to the following conclusions: (i) different hypothetical flow mechanisms lead to different patterns of strain relaxation with time; (ii) representative tissue properties show fluid drainage into the local microvasculature to be the dominant flow-related stress/strain relaxation mechanism; (iii) the relaxation time of strain in solid tumors due to drainage into the microvasculature is on the order of 5–10 sec.; (iv) under realistic applied pressure magnitudes, the magnitude of the strain relaxation can be as high as approximately 0.4% strain (4,000 microstrains), which is well within the range of strains measurable by elastography.

Physics in Medicine and Biology

[‡] Department of Mechanical, Aerospace and Nuclear Engineering, Rensselaer Polytechnic Institute, Troy, NY 12180

[§] Physics Department, Institute of Cancer Research, United Kingdom.

1. Introduction

Elastography refers to a collection of imaging techniques that allow mechanical strain distributions to be imaged and noninvasively quantified *in vivo*. The time scales over which the tissue response is typically measured ranges from about a millisecond (the typical duration for a radiation force “push pulse” [1, 2, 3]) to about one second, (the typical time scale of freehand quasistatic compression used in strain imaging [4, 5, 6]). Magnetic resonance elastography [7, 8] and sonoelasticity imaging [9, 10] typically use time-harmonic excitations with frequencies in the range of 10^2 Hz.

The mechanical responses of soft tissues and tissue mimicking gels observed under transient excitations, be they radiation force or time-harmonic excitations, show a predominantly elastic component as well as a small viscoelastic component. In quasistatic deformations, on the other hand, the strain fields are typically observed for about a second and are interpreted within the context of linear (or rarely nonlinear) elasticity. That is, the tissue response is assumed and observed to be approximately purely elastic.

Soft tissue is widely recognized as having both fluid and solid phases which can move independently of each other. Furthermore, the fluid exists within several “compartments” of the soft tissue, notably, the vasculature (including both the hemal and lymphatic vessels) and the extravascular space. Of course, due to permeability of microvessel walls in both vascular networks, fluid is often exchanged between these compartments. It is recognized that fluid flow leads to a stress relaxation at fixed strain (or conversely, a strain relaxation at fixed stress). It is reasonable to conjecture then, that by measuring the spatio-temporal patterns of strain in a strain-relaxation type of experiment, the effects of fluid flow can be visualized and measured. Indeed, recent experiments on a poroelastic tissue mimicking phantom [11, 12] have demonstrated the ability to image the effects of fluid flow on spatio-temporal strain patterns, and to interpret those effects within the biphasic [13, 14] or Biot poroelasticity [15] theory.

The linear “biphasic theory” [13, 14] can be regarded as a special case of Biot poroelasticity; the special case being that of two incompressible phases. It has been very successful at modeling the fluid-elastic coupling in cartilage [13, 14]. Cartilage tends to be avascular, however, and so fluid resides only in the “extravascular compartment”.

A different model for the mechanics of vascularized soft tissue, which includes the effects of fluid flow and the possibility of fluid exchange between fluid compartments was proposed in [16]. The model was originally developed in a rather general context to capture effects of fluid-elastic coupling in soft tissues, but was then applied to describe perfusion and drug delivery in solid tumors. It has since been validated in an experimental model in [17].

This paper can be seen as an extension to [11], in which similar questions are raised within the strictly biphasic context. Here we choose to emphasize, therefore, the role of the microvasculature in the stress relaxation of the solid. Our motivation for this work stems from the question *Can techniques from elastography be used to image spatio-temporal patterns of elastic strain and hence quantify interstitial fluid flow in soft tissues?* To answer this, we use the mathematical model of [16] in conjunction with finite element modeling to predict the effects of fluid flow on the spatio-temporal patterns of soft-tissue elastic strain under a variety of physiological conditions. The magnitude of the strain effects and their time scales dictate the measurability of the effects of fluid flow. Simulations relevant to a quasistatic elasticity imaging for the

characterization of fluid flow in solid tumors are emphasized here. In this context, the following questions are specifically addressed:

- (i) How do characteristics of tumor microvasculature, in particular the microvessel density and the leakiness of the microvessel walls, effect strain relaxation in solid tumors?
- (ii) How does the spatio-temporal strain pattern depend on the relative importance of fluid percolation through the extravascular compartment versus fluid exchange between the vascular and extravascular compartments?
- (iii) How does the choice of boundary conditions effect the spatio-temporal patterns of strain?

In the following “Methods” section, we describe a mathematical model that is used to address the questions enumerated above. We present an exact analytical solution of this model. The analytical solution serves the dual purpose of providing intuition and serving as a check on a finite element implementation. We then describe four computational experiments designed to answer the questions raised above. This is followed by Results, Discussion and Conclusions. In the Appendix, we include a derivation of the field equations and the exact analytical solution.

2. Methods

2.1. Mathematical Model

We use the mathematical model described in [16], and derived in Appendix A. The model treats the interstitial space as a biphasic material, and incorporates fluid exchange between the interstitial compartment and the microvasculature. It is this fluid exchange that distinguishes this model from a biphasic model for nonvascular soft tissues such as cartilage.

The assumptions that go into the model are small strains, small vascular space, Starling’s law for (transient) fluid transport across the vessel wall, Darcy’s law for fluid flow through the interstitial compartment, and Hooke’s law for the elastic response. It’s worth noting that we neglect the possible viscous behavior of the solid frame; such effects are studied in [18, 19], where, however, effects of fluid flow are neglected. We further assume the deformation takes place slowly enough that inertia can be neglected. Under these conditions (see Appendix A for details), the solid displacement vector \mathbf{u} and interstitial fluid pressure p are related by:

$$\nabla \cdot \dot{\mathbf{u}} - \nabla \cdot [\kappa \nabla p] + \chi p = 0 \quad 8.1 \quad (1)$$

$$\nabla \cdot [-p\mathbf{I} + \lambda \nabla \cdot \mathbf{u} \mathbf{I} + \mu(\nabla \mathbf{u} + (\nabla \mathbf{u})^T)] = 0 \quad 9.1 \quad (2)$$

Equation (1) represents a combination of the conservation of fluid mass in the interstitium, with the momentum equation for the fluid phase. Equation (2) represents the balance of total linear momentum in the tissue. The equations describe a “homogenized” medium, in which each elementary continuum element contains a large number of microvessels; thus we consider equations (1) and (2) to apply at a scales of $O(1 \text{ mm}^3)$, but not down to scales of $O(1 \text{ } \mu\text{m}^3)$. The symbols that appear in equations (1) and (2) are defined as follows: ∇ is the gradient operator; \mathbf{I} is the identity tensor; $\dot{\mathbf{u}} = \partial \mathbf{u} / \partial t$ is the solid phase velocity; p is the interstitial fluid pressure; κ is the interstitial permeability that governs the ease by which fluid percolates through the interstitium; λ and μ are the elastic Lamé parameters of the drained interstitium (also

called the solid matrix below); and χ is the average microfiltration coefficient, given by $\chi = \chi_V + \chi_L$, with $\chi_V = \frac{L_p S_V}{V}$ and $\chi_L = \frac{L_{pL} S_L}{V}$; L_p (resp. L_{pL}) is the hydraulic conductivity of the hemal (resp. lymphatic) capillary wall, S_V/V (resp. S_L/V) is the surface area of the hemal (resp. lymphatic) capillary wall per unit volume of tissue. In the special case $\chi = 0$, we recover the linear biphasic equations describing the deformation of avascular cartilage like materials.

It is implicit in Equations (1) and (2) that, in general, mechanical loading not only strains the tissue, but also pressurizes both the solid and fluid phases. The pressurization mechanism can be understood in terms of the mechanical behavior of the drained interstitium, also called the elastic solid matrix. In contrast to the solid phase which we assume to be incompressible, the solid matrix is compressible; the pore space within the solid matrix allows its overall volume to change with applied mechanical loading. In an idealized context, where the saturating fluid can move frictionlessly within the pore system and thus drain freely and instantaneously, the pore system would shrink instantaneously in response to an applied loading. Real viscous interstitial pore fluid, however, faces resistance to percolation and drainage. It thus resists pore system shrinking, thereby pressurizing and being pressurized by the solid phase. After the sudden application of an applied compression, pressure relaxation takes place, i.e., interstitial fluid pressure drops gradually, as the interstitial fluid percolates or drains gradually in response to the pressurization. During the relaxation the tissue approaches static equilibrium for the solid matrix. At static equilibrium, the interstitial fluid pressure vanishes, $p = 0$, and the mechanical behavior is governed by the solid matrix Lamé parameters. It follows from the assumption that both solid and fluid phases are incompressible that dilatation can occur only when the corresponding volume of fluid percolates or drains from the interstitial compartment.

2.1.1. One dimensional analytical solution Solutions of equations (1) and (2) exhibit various stress/strain relaxation behaviors. Insight into these behaviors and their connection to different physical constants and mechanisms that appear in the governing equations may be developed by examining a simple analytical solution. This analytical solution also serves as a check on the validity of our finite element (FEM) numerical implementation.

For the purposes of developing an analytical benchmark solution, we consider a 2D plane strain scenario of a rectangular homogeneous tissue sample in an unconfined compression test. The configuration is shown schematically in Figure 1. The sample has dimensions of $L \times h$ and fluid can flow freely across the lateral boundaries ($p = 0$), which are also traction free. The fluid cannot flow across the top and bottom boundaries, which are also shear stress free (slip boundary conditions). $u_y = 0$ at the bottom while a displacement step (or ramp) function is applied at the top.

For a step function compression of magnitude u_0 , the pressure field in the sample is given by (equation (B.5) in Appendix B)

$$p(x, t) = \frac{4\mu u_0}{Lh} \exp(-\chi(\lambda + 2\mu)t) \times \sum_{n=1}^{\infty} \left(\frac{\beta_n}{\alpha_n}\right) \sin(\alpha_n x) \exp(-\alpha_n^2 \kappa(\lambda + 2\mu)t) \quad 17.1 \quad (3)$$

Here, $\alpha_n = \frac{n\pi}{L}$, $\beta_n = 1 - (-1)^n$.

Note that the pressure relaxation associated with microvascular filtration, $\exp(-\chi(\lambda + 2\mu)t)$, is uniform over the entire sample. This is the result that a uniform vascular distribution (as assumed in this example) drains all parts of the tissue at the same rate. The pressure relaxation associated with fluid percolation (the $\exp(-\alpha_n^2\kappa(\lambda + 2\mu)t)$ factor), on the other hand, is nonuniform over the sample. The exponential factor is different for each n in the sum, and each factor multiplies a spatial “mode shape” $\sin(\alpha_n x)$. Thus each spatial mode decays at a different rate. While the mode shapes in this example are relatively simple, in general they depend on the sample geometry and boundary conditions.

The horizontal normal strain, ϵ_{xx} , behaves very similarly to the pressure in this example. Equation (B.3) shows

$$(\lambda + 2\mu)\epsilon_{xx} = p(x, t) - \lambda\epsilon_{yy} = p(x, t) - \lambda\frac{u_0}{h} \quad p3 \quad (4)$$

Thus in this simple example, the spatio-temporal behavior of the interstitial pressure p is reflected directly in the lateral strain distribution.

The above expressions are valid for a step compression applied instantaneously with time. The principal of linear superposition allows us to integrate in time equation (3) to obtain the response for a gradual compression of the sample. In particular, (see Appendix B for details) for an overall compression u_0 applied linearly with time over an interval of time t_1 , the pressure distribution is very similar in form to (3); *viz.*

$$\begin{aligned} p(x, t) &= \frac{4\mu u_0}{Lht_1} \exp(-\chi(\lambda + 2\mu)t) \\ &\quad \times \sum_{n=1}^{\infty} A_n \sin(\alpha_n x) \exp(-\alpha_n^2\kappa(\lambda + 2\mu)t) \quad \text{for } t \geq t_1. \quad 1752 \\ A_n &= \frac{\beta_n [\exp((\alpha_n^2\kappa + \chi)(\lambda + 2\mu)t_1) - 1]}{\alpha_n(\alpha_n^2\kappa + \chi)(\lambda + 2\mu)} \quad 17.3 \quad (6) \end{aligned}$$

The lateral strain is again given in terms of the pressure by equation (4).

Equations (5) and (4) indicate that the strain in x -direction (ϵ_{xx}) reaches its maximum right after the mechanical loading has been applied and then decreases with time, as the tissue relaxes. This is a typical pattern in *unconfined* tests of poroelastic samples, and can be understood by considering the configuration assumed by the sample in the two limits, $t = 0^+$ and $t = \infty$. Immediately after a step mechanical loading has been applied ($t = 0^+$), fluid has not yet had a chance to leave the sample. Thus, at $t = 0^+$, we expect the sample to behave like an incompressible solid, i.e., it occupies the same volume (area) as it occupied previously. On the other hand, when the tissue is completely relaxed ($t = \infty$), the pressure relaxes to zero and the mechanical behavior is governed by the solid matrix Lamé parameters. Since the solid matrix is compressible, the sample should now occupy a smaller volume (area). As u_y is constant with time in this experiment, (due to the constant boundary conditions), any volume reduction must be reflected in a shrinking in the x direction. Of course, during the transient regime, while the fluid is exuding and/or draining, all the configurations assumed by the sample correspond to configurations between these two extremes.

As mentioned above, in both equations (3) and (5) we can identify in two different transient phenomena, percolation and vascular drainage. These are controlled by $\alpha_n^2\kappa(\lambda + 2\mu)$ and $\chi(\lambda + 2\mu)$, respectively. The form of these constants indicates that, beside the dependence on the interstitial permeability and filtration coefficient, the

greater λ and μ are (especially λ which usually is much larger than μ), the faster the tissue relaxes. The ratio of κ/L^2 and χ indicates the relative importance of fluid flow within the extravascular compartment versus fluid exchange between compartments.

To illustrate this, we plot in Figure 2 the solution for pressure p (Equation (B.7)), at three different times; the parameters used were $L = 10\text{cm}$, $h = 10\text{cm}$, $u_0 = 1\text{cm}$ and $t_1 = 0.3\text{sec}$. For the blue line, the poroelastic parameters are chosen such that vascular drainage, or fluid exchange between compartments, is the dominant phenomenon. (The parameters used are listed in Table I and correspond to the inclusion in Experiment 1.) We observe that the pressure is homogeneous along almost the whole sample width. The pressure decreases very rapidly close to the lateral surfaces, which indicates that only a small amount of fluid crosses the boundary. For the red line, we increase κ 10,000 times and decrease χ 1,000 times. Now, we see that the pressure boundary layer rapidly becomes thicker with time, indicating that percolation is now dominant. In Figure 3 we plot the strain field, ϵ_{xx} , at $t = 5.4\text{sec}$, for both cases. In the Figure 3(a), in agreement with the pressure field plotted in Figure 2 (blue solid line), we see that the strain is approximately constant along almost the whole sample. Again, this indicates that the vascular drainage is dominant and percolation is negligible outside the very thin boundary layers located at the sample sides. It means that ϵ_{xx} is decreasing at the same rate everywhere in the sample. In Figure 3(b) we see that the strain varies with x , indicating that percolation is now important. In agreement with [14, 11, 12], it indicates that now the shrinking in the x direction *diffuses* with time from the lateral sides toward the center. It is interesting to note that at $t = 0^+$ and $t = \infty$ the sample configurations are the same in both cases, the difference being in how the samples go from one limit to the other.

2.1.2. Selection of material properties The vascular poroelastic medium is defined by four physical parameters: λ , μ , κ and χ . We expect several of the biomechanical properties of solid tumors to be altered from those in normal host tissue. In particular, we expect angiogenesis to lead to higher than normal microvascular filtration coefficient, χ , due to higher than normal microvessel density (and thus elevated S_V/V) and leakier than normal microvessel walls (and thus elevated L_p). Furthermore, we expect the shear modulus μ to be elevated in solid tumors. Finally, measurements indicate [20] that the interstitial permeability tends to be higher in malignant solid tumors than in normal tissues. This may be due to the heterogeneity typical of tumor stroma which creates atypically large pores which offer low resistance to fluid flow.

The numerical values selected for κ and χ were chosen according to values used in [20]. The only known measurement for χ in a tumor indicates it is elevated by a factor of 10 – 1000 over normal values [21]; we chose a conservative factor of 30 in our simulations. We note that [20] reports a range κ values over an order of magnitude for different breast tumor types. In Experiment 3, we arbitrarily increased the background interstitial permeability, κ , to highlight percolation effects and explore sensitivity to this parameter.

The value for μ used in [20] is inappropriately low for breast tissue. Instead we use values reported in [22]. Of course, the shear modulus of “normal” breast tissue can vary according to tissue type (e.g. glandular or adipose), patient age, etc. The value considered here is consistent with the order of magnitude of the measurements reported in [23, 24, 25]. Given μ , we calculate the corresponding value for λ by assuming a specific value for Poisson’s ratio of the solid matrix, ν . For normal tissue,

we choose $\nu = 0.49$. This value of ν corresponds to a porosity of about 0.02, which is a low estimate; higher porosities lead to lower Poisson's ratios. For tumor tissue, we choose $\nu = 0.47$, which corresponds to a porosity of roughly 0.06. These values for ν are expected to lead to an underestimate of the magnitude of the strain relaxation effects. All the parameters used in the simulation are summarized in Table I.

2.2. Computational experiments

In order to evaluate the predictions of the mathematical model with nontrivial geometries and boundary conditions, we developed a finite element discretization of equations (1) and (2) in two dimensions. We used the standard Galerkin approximation with bilinear shape functions for both the pressure and displacement fields. To integrate in time we use the Backward Euler method, assuming all material parameters are constant with time. We have validated our implementation by comparing the numerical solution to the analytical solution derived in the previous section, as shown in the Figure 2.

We now use this finite element implementation to study two dimensional problems that model hypothetical clinical imaging exams. In the computational experiments presented here, we have attempted to reproduce hypothetical configurations for clinical breast exams, while making some modeling simplifications. For example, we considered a rectangular domain and a plane strain deformation state. In addition we assumed homogeneous properties, except for an isolated circular inclusion. The properties of the inclusion are chosen to model a malignant tumor.

2.2.1. Experiment 1 Experiment 1 is schematically shown in Figure 4. The circular inclusion has 1 cm diameter and the sample has dimensions 10cm \times 10cm. The fluid *cannot* flow across the boundaries, mimicking a portion of tissue *completely* bounded by skin. Therefore, the interstitial fluid can redistribute, but the only way for it to leave the sample is by vascular drainage. Such an idealized boundary condition is valid when the drainage effects are much larger than the percolation effects and the permeable boundary is relatively far away from the region to be investigated, as in the case here. The tissue is fixed at the bottom, where $u_x = u_y = 0$. The lateral surfaces are traction free. At the top, we simulate the mechanical loading from a compressor of 5 cm width. The displacement of the compressor is modeled by a ramp function such that the prescribed u_y goes from 0 to 1 cm in 0.3 sec, in the region corresponding to $x = 2.5\text{cm}$ to $x = 7.5\text{cm}$. Below the compressor we prescribe zero shear stress (τ_{yx}), which models a slip boundary condition.

2.2.2. Experiment 2 Experiment 2 is schematically shown in Figure 5. The size of the circular inclusion and the background are unchanged from Experiment 1, and as before, the fluid cannot flow across the boundaries and the tissue is fixed at the bottom. Now, however, the model is completely confined at the top, where u_y goes from 0 to 0.03cm in 0.3sec, and is partially confined at the lateral surfaces, i.e., $u_x = 0$ from $y = 2.0\text{cm}$ to $y = 10\text{cm}$, while it is traction free from $y = 0.0\text{cm}$ to $y = 2.0\text{cm}$. The goal here is to reproduce a situation of partial breast confinement, with the recognition that the breast is not completely confined in the clinical setting.

2.2.3. Experiment 3 Experiment 3 has the same configuration as Experiment 1, but the interstitial permeability, κ , is the same for both inclusion and surrounding tissue

and is $6.4 \times 10^{-13} \text{m}^2 / (\text{Pa} \cdot \text{sec})$.

2.2.4. Experiment 4 Experiment 4 has the same configuration as Experiment 1, however the fluid can flow freely across the lateral surfaces of the sample, where $p = 0$.

3. Results

We solved the problems just described using bilinear finite elements on a $1,000 \times 1,000$ mesh, and backward Euler time marching with a time step of 0.03 secs . In this section we show results corresponding to the region delimited by the dotted line in Figures 4 and 5. It has dimensions of $4 \text{ cm} \times 4 \text{ cm}$ and is contained between $x = 3.0 \text{ cm}$ to $x = 7.0 \text{ cm}$ and $y = 5.5 \text{ cm}$ to $y = 9.5 \text{ cm}$. We emphasize that we have solved the problem in the entire domain, but are showing the results only in this region of interest, in order to investigate the behavior of the inclusion and its surroundings in detail. This is intended to be representative of ultrasound imaging where the physical boundaries are typically distinct from the image boundaries.

3.1. Experiment 1

In this experiment, the fluid exchange between interstitial and microvascular compartments is the dominant phenomenon. Due to the difference between the filtration coefficient inside and outside the inclusion (it is 30 times larger inside), a transient analysis of the problem can be outlined considering two different time scales: the inclusion's relatively short relaxation time and the surrounding tissue's large relaxation time.

Right after the mechanical loading has been applied and before significant fluid drainage has occurred, the tissue is pressurized and the sample approximately behaves like an incompressible elastic solid, with the same shear modulus (μ) as the corresponding solid matrix and a Young's modulus equal to 3μ .

In Figures 6(a)-6(c) we plot the pressure field at $t = 0.3 \text{ sec}$, 5.4 sec , 10.2 sec . Figure 6(a) corresponds to $t = 0.3 \text{ sec}$, which is immediately after the compression ramp. We can see the stress concentrations at the transducer edges radiating in the upper left and right corners of the figure. At the center, we can distinguish the inclusion and four lobes resulting from the stress concentration at the inclusion. Gradually, as the fluid drains from the interstitium to the microvasculature, the tissue relaxes. Comparing Figures 6(a) and 6(b) shows that the inclusion relaxes much faster than the surrounding tissue. This may be attributed to the higher value of the microvascular filtration coefficient in the inclusion. The inclusion takes about 10 secs to relax almost completely. In the Figure 6(c) we see that the pressure inside the inclusion has nearly reached its equilibrium value ($p \approx 0$).

Fluid flow is necessarily accompanied by a local volume change, measured by the dilatation, $\Delta = \epsilon_{xx} + \epsilon_{yy} + \epsilon_{zz}$. (Recall that we are working with the plane strain approximation, in which $\epsilon_{zz} = 0$.) To emphasize the transient aspect of fluid flow, we plot the difference in dilatation at two times in Figures 6(d) and 6(e). Figure 6(d) shows $\Delta(t = 5.4 \text{ sec}) - \Delta(t = 0.3 \text{ sec})$. We see significant volume change within the highly vascularized inclusion and little change outside it. The volume change reflects the fact that a relatively large amount of fluid has drained from the vascular inclusion, while relatively little has left the background within the 5 sec time period. After 10 sec

or so, fluid flow has all but ceased. This is seen in Figure 6(e), which shows practically no volume change between $t = 15.0 \text{ sec}$ and $t = 10.2 \text{ sec}$.

Typically in ultrasound elastography only a single component of strain is measured. For that reason, we show in Figures 6(f) and 6(g) the “vertical” strain component (in the direction of dominant compression; ϵ_{yy}) corresponding to the dilatations shown in Figures 6(d) and 6(e). That is, Figure 6(f) shows $\epsilon_{yy}(t = 5.4 \text{ sec}) - \epsilon_{yy}(t = 0.3 \text{ sec})$, and Figure 6(g) shows $\epsilon_{yy}(t = 15.0 \text{ sec}) - \epsilon_{yy}(t = 10.2 \text{ sec})$. While Figure 6(d) shows nearly uniform distribution of dilatation, figure 6(f) shows that such uniformity is lost when examining a single strain component. Nevertheless, we see in Figure 6(g) that relaxation due to fluid flow has all but ceased after about 10 sec .

Both Figures 6(e) and 6(g) show that the interstitial fluid drains faster (or percolates) in a thin region around the inclusion, due to the stress concentration. In particular, we notice crescent shaped regions at the top and bottom of the inclusion. In these same locations in Figure 6(c) we see very steep pressure gradients driving fluid toward the highly vascularized inclusion where it can be drained by the microvasculature.

The pressure in the background region takes about 300 sec to relax almost completely. As discussed before, at the steady state, where both inclusion and surrounding tissue are relaxed, the sample assumes the configuration where the mechanical behavior of both inclusion and surrounding tissue are governed by the respective solid matrix Lamé parameters.

3.2. Experiment 2

Recall that here the boundary conditions are selected to approximate conditions of confined compression. As before, the fluid exchange between interstitial and microvascular compartments is the dominant phenomenon. A transient analysis of the problem can again be outlined by considering two different time scales.

In Figures 7(a)-7(c) we plot the pressure field at $t = 0.3 \text{ sec}$, 6.3 sec , 13.5 sec . The pressure field at $t = 0.3 \text{ sec}$ is shown in Figure 7(a). We see that the pressure magnitude is similar to the previous case (Figure 6(a)) despite the much smaller displacement prescribed at the top boundary. This is obtained by confining a portion of the lateral surface. We also observe that in contrast to the previous case, there is no stress concentration in the upper left and right corners and the pressure field is almost uniform.

As the interstitial fluid drains, the inclusion relaxes. The pressure field at $t = 6.3 \text{ sec}$ is shown in Figure 7(b). We can see that the pressure inside the inclusion is about 85% smaller at $t = 6.3 \text{ sec}$ than at $t = 0.3 \text{ sec}$, while it remains close to the peak in the surrounding tissue. Once again this is due to the higher vascular filtration in the inclusion. The inclusion takes about 10 sec to relax almost completely. The pressure field for $t = 13.5 \text{ sec}$ is shown in Figure 7(c). The pressure inside the inclusion is now slightly negative. At this point, the relaxation of the surrounding tissue tends to expand the inclusion, thus pulling fluid back into the inclusion interstitial compartment from the microvasculature. In fact, the inclusion attains its smallest volume at approximately $t = 13.5$ and then swells until the sample reaches the steady state configuration.

In Figures 7(d) and 7(e) we plot $\Delta(t = 6.3 \text{ sec}) - \Delta(t = 0.3 \text{ sec})$ and $\Delta(t = 31.5 \text{ sec}) - \Delta(t = 13.5 \text{ sec})$. These show the change in dilatation with time. Figure 7(d)

shows that initially, the inclusion drains quickly. Figure 7(e) shows that eventually, the inclusion starts to slowly reabsorb fluid while the background continues to drain.

Figures 7(f) and 7(g) show the vertical strain ϵ_{yy} corresponding to the dilatation fields shown in Figures 7(d) and 7(e). As in the previous experiment we see the four lobes resulting from the stress concentration redistribution around the inclusion.

3.3. Experiment 3

In this experiment we investigate the impact of increasing the interstitial permeability, on the spatio-temporal strain pattern. The permeability here is 100 times higher than in the previous cases, and is the same for both background and inclusion. The boundary conditions are selected to approximate unconfined compression, as in Experiment 1.

In Figures 8(a)-8(c) we plot the pressure field at $t = 0.3 \text{ sec}, 5.4 \text{ sec}, 10.2 \text{ sec}$. These appear to be roughly smoothed versions of the corresponding distributions shown in Figures 6(a)-6(c). Thus, again the inclusion reaches equilibrium much more quickly than the surroundings, even though they have the same permeability. (The microvascular filtration coefficient in the inclusion is still a factor of 30 elevated over the background value.)

In Figures 8(d) and 8(e) we plot $\Delta(t = 5.4 \text{ sec}) - \Delta(t = 0.3 \text{ sec})$ and $\Delta(t = 15.0 \text{ sec}) - \Delta(t = 10.2 \text{ sec})$. These show the change in dilatation with time. Figures 8(d) and 8(e) are not smoothed versions of the corresponding Figures 6(d) and 6(e). We see, especially in comparing Figures 6(e) and 8(e), that the high pressure gradients above and below the inclusion are much more effective at moving fluid through the interstitium in this case than in the case with the lower interstitial permeability. Indeed, a slow propagation of dilatation may be seen traveling away from the inclusion, beginning at the crescent shaped regions. This effect could have been anticipated by the increase of the interstitial permeability, and is corroborated in the numerical results. The more complicated dilatation patterns seen in this experiment correspond to still more complicated normal strain patterns, shown in Figures 8(f) and 8(g).

The pressure in the background region takes about 300 sec to relax almost completely. This is the same as for Experiment 1; that is, the relaxation time is roughly independent of the interstitial permeability coefficient. At the steady state, the sample assumes the same configuration as in Experiment 1.

3.4. Experiment 4

This experiment is identical to Experiment 1, except now the lateral surfaces are permeable ($p = 0$). In the Figure 9(a), (b) and (c) we plot the pressure field at $t = 0.3, 5.4$ and 10.2 sec , respectively. We plot the solution in the entire domain because the only change, when compared with Experiment 1, is the appearance of thin boundary layers along the lateral surfaces. Due to the small interstitial hydraulic conductivity, the effect of the permeable boundary condition is confined to this thin layer.

4. Discussion

In Experiment 1, we observe that in the first 5 seconds the inclusion relaxes much more than the surrounding tissue. During this time, its volume reduces by about 4,000

microstrains. For an inclusion of 1cm diameter this implies displacements of the order of 40 microns. On the other hand, after the inclusion stops relaxing, the surrounding tissue relaxation becomes the predominant phenomenon. Since drainage is the main relaxation mechanism for both inclusion and surrounding, their relaxation time scales are directly proportional to the respective filtration coefficient values and, as seen in Equations (B.5)-(B.8), can be roughly estimated by $\tau = 1/\chi(\lambda + 2\mu)$, ($\approx 3 \text{ sec.}$ in this example for the inclusion; $\approx 90 \text{ sec.}$ for the background.) This time scale is consistent with the time scale of fluid filtration observed in [20]. The shrinkage magnitude resulting from the relaxation is directly proportional to the applied displacement at the boundary. The constant of proportionality is directly related to Poisson's ratio; the smaller the solid matrix Poisson's ratio, the larger the shrinking.

Both Experiments 1 and 2 can be idealized as two different relaxation processes. Initially the deformation of the both inclusion and background can be thought of as incompressible. After the compression is applied, the material begins to relax by changing its volume as fluid is forced out. The relaxation of inclusion takes place relatively rapidly compared to that in the background. Thus, during the relaxation of the inclusion, we may think of the background as incompressible. So initially, i.e. during the first 5sec or so, we may think of the system as relaxing towards an equilibrium corresponding to a compressible inclusion in an incompressible background. On longer time scale, the background relaxes allowing its volume to change. This slower relaxation corresponds to the relaxation toward a compressible background and compressible inclusion.

In terms of quantitative strain magnitudes, we see in Experiment 2 that in the first 6 seconds the inclusion shrinks about 4,000 microstrains, which, again, for an inclusion of 1cm diameter implies displacements of the order of 40 microns. The shrinkage magnitude is determined by the applied displacement, the unconfined to confined lateral area ratio, and the inclusion solid matrix *bulk modulus*. In the limit case, where the sample is completely confined, practically all the sample's volume reduction resulting from the applied displacement must be reflected in the inclusion's volume reduction. We observed also that after the inclusion relaxes it experiences a gradual swelling, while the surrounding relaxation takes place. It can be understood by reconizing that the surrounding tissue shrinks as it relaxes, because its solid matrix is compressible. The shrinking is partially balanced by the inclusion's swelling. Again, in the limit case, where the sample is completely confined, all the shrinking must be balanced by the inclusion's swelling.

In Experiment 3, we can observe that raising the interstitial permeability by a factor of 100 had a small effect on the spatio-temporal patterns of strain, especially before about 5 seconds. In a comparison with Experiment 1, we observe that the pressure field is no longer homogeneous inside the inclusion, decreasing from the periphery toward the center, indicating that part of the drained fluid is being replaced (at the periphery) by fluid flowing from the surroundings. For the same reason, part of the surrounding tissue close to the inclusion experiences now a larger dilatation. The impact is larger on intermediate and longer time scales, especially around the inclusion. There we could see the dilatation partially "diffusing" from the center of the sample toward the boundaries. Here, an analogy can be made with what is discussed in Section 2.2, where now the inclusion's boundaries play the role of the open lateral boundaries in Figure 2.

In a case where the interstitial permeability is as important as (or more important than) the filtration coefficient, a transient analysis of the problem could no longer

be outlined considering two different time scales - the inclusion's relatively short relaxation time and the surrounding tissue's large relaxation time - despite the difference between the filtration coefficient inside and outside the inclusion. The whole sample would relax approximately with the same rate due to the fluid replacement mechanism discussed above.

The effect of letting the fluid flow freely across the lateral boundaries in Experiment 4 is imperceptible inside the region of interest investigated in the previous experiments. In fact, its effect is only felt in a very thin region close to the sample's lateral sides, similarly to what is discussed in Section 2.2. This is, of course, consistent with the notion that the fluid exchange between compartments is much more important than the fluid flow within the extravascular compartment. However, in cases where the interstitial permeability is significant, permeable boundaries become important.

The results suggest that it may be possible to image properties related to the interstitial fluid motion in tissue matrix by measuring the corresponding strain rate. A sequence of images acquired from ultrasound or other scanners could be processed, as they are in elasticity imaging, to track the spatio-temporal patterns of elastic strain. In addition, the strain pattern could then be used to solve for the spatial distribution of the poroelastic parameters, in particular, the shear modulus μ and the microvascular filtration coefficient χ .

It is interesting to consider the ultrasound measurability of the transient strains predicted here. In experiment 1, we noted a volume change in the inclusion of about 0.4% after 5 seconds, in an overall compression of 10%. Such a relaxation would certainly be measurable by ultrasound, though tracking a compression over a full 10% strain might present technical difficulties. On the other hand, in experiment 2, with confined compression of 0.3% we noted the same inclusion volume change of 0.4% over about 6 seconds. The volume change is roughly isotropic in the plane, so about half that of that, or about 0.2%, would take place in the high resolution (ultrasound propagation) direction. In practice, it's likely that the plane strain assumption would be violated here, and the volume change might be expected to be isotropic in the volume. In that case, only about 1/3 of the total volume change, or about 0.15% strain, would be reflected in the high resolution direction. This magnitude of strain, over 6 seconds, would certainly be a measurable effect.

The time scale of inclusion relaxation is expected to be of the order of magnitude expected in a tumor a high density of leaky microvessels. This implies that for compressions and observations significantly faster than 5 – 6 seconds or so, there is little danger that fluid redistribution can cause an operator to wrongly interpret a strain image as related to elastic effects only. On the other hand, slow acquisitions as might be associated with 3D systems, might see “fluid redistribution strain artefacts,” i.e. strain contributions due to fluid redistribution within the tissue. These artefacts would more significantly effect tumors with high vascularity than “normal” tissues.

Whether the magnitudes of the effects predicted here might be seen in clinical practice depends on the validity of several assumptions. First, these magnitudes depend on the validity of the parameters chosen for the model. These are selected as described above, and may be assumed to have large variability in practice. Our model assumes a linear response to the applied pressure. This implies, among other limiting situations, that neither the porosity nor permeability will change with applied pressure. It is likely that this second order effect will indeed remain small provided the applied pressure in the tissue stays well below the collapse pressure of the microvasculature. In experiment 2, for example, the maximum pressure observed

was about 3KPa (about 22mmHg) which is about the same magnitude as typical capillary blood pressure. Therefore, in this case we would not expect to temporarily collapse the microvasculature in the tissue. In experiment 1, on the other hand, the maximum pressure observed was about $5 - 6\text{KPa}$ (approx 40mmHg). Whether the microvasculature would collapse in this case or instead would remain open by fluid forced into it cannot be determined by our model. Our model neglects all forms of transient solid response that is not directly related to fluid flow (that is, it neglects viscoelasticity). The magnitude of these possible effects is impossible to estimate at this time. Finally, the plane strain assumption is taken as analytically convenient for our purposes, but is not supposed that it is quantitatively accurate. Quantitative discrepancies between $2D$ and $3D$ predictions of as much as 50% might reasonably be expected, though neither order of magnitude changes nor qualitative changes would be expected.

5. Conclusions

A poroelastic model that includes the effects of fluid flow and the possibility of exchange between fluid compartments was used in conjunction with finite element modeling to predict the effects of fluid flow on the spatio-temporal patterns of soft-tissue elastic strain under a variety of physiological conditions.

The analytical solution for the problem consisting of a macroscopically homogeneous tissue sample in an unconfined test show two different transient phenomena, percolation and drainage, controlled by $\hat{\kappa}$ and $\hat{\chi}$, respectively. In soft tissues drainage is the dominant phenomenon.

Numerical simulation results suggest that it may be possible to image properties related to the interstitial fluid motion and the solid tissue matrix in tissues by measuring the corresponding strain rate. Further, they show that the abnormal tumor microvasculature may increase the strain relaxation rate.

The total dilatation resulting from the tissue relaxation is controlled by the Poisson's ratio. We didn't perturb significantly the spatio-temporal patterns of strain by increasing the interstitial permeability by 100 times; this is especially true during the time period while the inclusion relaxes. The effect of letting the fluid freely flow across the lateral boundaries is confined to a very thin region close to the flow boundaries.

Acknowledgments

This work has benefited tremendously from the authors' discussions with Dr. G.P. Berry. The authors are indebted to Prof. M.F. Insana for making available references [18, 19] in advance of their publication. This research was partially funded by USAMRAA Grant W81XWH-04-1-0763, and by NSF.

Appendix A. Derivation of field equations

In this section we present a rederivation of the field equations from [16]. Figure 10 represents schematically a portion of soft tissue interstitium. Its boundary and domain are denoted by Γ and Ω , respectively. The interstitial boundary, Γ is comprised of three parts: the outer boundary Γ_o , the interface with the hemal capillaries Γ_c , and the interface with the lymphatic capillaries Γ_L . We regard the interstitial

compartment as a linear biphasic solid-fluid mixture, where both fluid and solid phases can move independently of each other. The two phases are treated as intrinsically incompressible. Thus the total stress in interstitium, $\boldsymbol{\sigma}^t$, is given by:

$$\boldsymbol{\sigma}^t = -p\mathbf{I} + \lambda\nabla \cdot \mathbf{u}\mathbf{I} + 2\mu\nabla^{Sym}\mathbf{u} \quad 5 \quad (\text{A.1})$$

Here λ and μ are the *solid matrix* Lamé parameters, p is the interstitial fluid pressure, and \mathbf{u} is the displacement of the solid phase. The infinitesimal strain tensor is given by $\boldsymbol{\epsilon} = \nabla^{Sym}\mathbf{u} = \frac{1}{2}(\nabla\mathbf{u} + (\nabla\mathbf{u})^T)$. Note that, in contrast to the solid phase, the *solid matrix* is compressible.

For frequencies and rates of strain which occur physiologically, and under many clinical applications, the effects of inertia in tissue dynamics may be neglected. Under this assumption and in the absence of body forces, the resulting momentum equations for the fluid phase and mixture may be written as ([14] and [26]):

$$\nabla \cdot \boldsymbol{\sigma}^f + \kappa^{-1}\dot{\mathbf{w}} = 0 \quad 3 \quad (\text{A.2})$$

$$\nabla \cdot \boldsymbol{\sigma}^t = 0 \quad 4 \quad (\text{A.3})$$

Here, $\boldsymbol{\sigma}^f = -p\mathbf{I}$ is proportional to the stress in the fluid phase, κ is the interstitial permeability, and \mathbf{w} is volume average relative fluid displacement (relative to the solid matrix). Equation (A.2) is a statement of Darcy's law for the fluid flow through the interstitium, while equation (A.3) is a statement of conservation of total linear momentum.

For a biphasic material with incompressible phases, the equations (A.1), (A.2) and (A.3) are augmented by the incompressibility constraint for the fluid phase:

$$\nabla \cdot \dot{\mathbf{u}} + \nabla \cdot \dot{\mathbf{w}} = 0 \quad \text{paul6} \quad (\text{A.4})$$

To bring out explicitly the effects of the vascularization, we shall average (A.4) over an elementary "averaging volume", that is, a small volume (typically $O(1mm^3)$), which is large enough to contain a sufficiently large number of microvessels that the averages below become sensibly stationary.

To that end, we integrate (A.4) over Ω , our averaging volume:

$$\int_{\Omega} \nabla \cdot \dot{\mathbf{u}} dV + \int_{\Omega} \nabla \cdot \dot{\mathbf{w}} dV = 0. \quad \text{paul7} \quad (\text{A.5})$$

We apply the divergence theorem to the second term in equation (A.5) to obtain:

$$\int_{\Omega} \nabla \cdot \dot{\mathbf{u}} dV + \int_{\Gamma_0} \mathbf{n} \cdot \dot{\mathbf{w}} dS + \int_{\Gamma_c} \mathbf{n} \cdot \dot{\mathbf{w}} dS + \int_{\Gamma_L} \mathbf{n} \cdot \dot{\mathbf{w}} dS = 0. \quad \text{paul8} \quad (\text{A.6})$$

Here, we recall that divided the total boundary of the interstitial space into three parts, the external boundary Γ_0 , the (hemal) capillary surface Γ_c , and the lymphatic capillary surface, Γ_L .

The last two terms in equation (A.6) represent fluid fluxes into the microvessels. As such, they can be related to the pressure difference across the microvessel wall through Starling's law applied to both classes of microvessels:

$$J_c = L_p(p_v - p) \quad \text{paul9} \quad (\text{A.7})$$

$$J_L = L_{pL}(p_L - p) \quad \text{paul10} \quad (\text{A.8})$$

Here J is the volume fluid flux out of the vessel, L_p represents the hydraulic conductivity of the microvessel wall, and the subscripts c and L denote hemal capillaries and lymphatic capillaries, respectively. p_v and p_L thus represent the hemal capillary and lymphatic capillary pressures, respectively.

Using equations (A.7) and (A.8) allows us to make the following approximations:

$$\int_{\Gamma_c} \mathbf{n} \cdot \dot{\mathbf{w}} dS \approx L_p S_v (p - p_v) \quad \text{paul11} \quad (\text{A.9})$$

$$\int_{\Gamma_L} \mathbf{n} \cdot \dot{\mathbf{w}} dS \approx L_{pL} S_L (p - p_L) \quad \text{paul12} \quad (\text{A.10})$$

Here, S_v and S_L are the total surface areas of the two classes of microvessels within the averaging volume, Ω .

Further, ensemble averaging the first and second terms of (A.6) over all representative realizations of the microvasculature yields:

$$\int_{\Omega} \nabla \cdot \dot{\mathbf{u}} dV \approx V \nabla \cdot \langle \dot{\mathbf{u}} \rangle \quad \text{paul13} \quad (\text{A.11})$$

$$\int_{\Gamma_0} \mathbf{n} \cdot \dot{\mathbf{w}} dS \approx \int_{\Gamma_0} \mathbf{n} \cdot \langle \dot{\mathbf{w}} \rangle dS = \int_{\Omega} \nabla \cdot \langle \dot{\mathbf{w}} \rangle dV = V \nabla \cdot \langle \dot{\mathbf{w}} \rangle \quad \text{paul12} \quad (\text{A.12})$$

Angle brackets in (A.11) and (A.12) represent ensemble averages. We now drop the angle brackets with the understanding that all symbols represent quantities averaged over the microstructure. V is the volume of Ω .

We now use (A.9-A.12) in (A.5) to write:

$$\nabla \cdot \dot{\mathbf{u}} + \nabla \cdot \dot{\mathbf{w}} + \chi_v (p - p_v) + \chi_L (p - p_L) = 0 \quad \text{paul15} \quad (\text{A.13})$$

$$\chi_v = \frac{L_p S_v}{V} \quad \text{paul16} \quad (\text{A.14})$$

$$\chi_L = \frac{L_{pL} S_L}{V} \quad \text{paul17} \quad (\text{A.15})$$

Equation (A.13) is identical to Equation 4 in [16] with appropriate reinterpretation of average fluid and solid displacements. At normal physiological conditions, where $p_v > p > p_L$, $\chi_v(p_v - p)$ and $\chi_L(p - p_L)$ represent the transcapillary flow and the lymphatic drainage, respectively.

Transcapillary exchange and lymphatic drainage can be expected to be taking place continuously in living tissues. Under these ‘‘steady state operating conditions,’’ p and \mathbf{w} will in general be nonzero. Therefore, we let

$$\mathbf{u} = \mathbf{u}^{ss} + \tilde{\mathbf{u}} \quad \text{paul19} \quad (\text{A.16})$$

$$\dot{\mathbf{w}} = \dot{\mathbf{w}}^{ss} + \dot{\tilde{\mathbf{w}}} \quad (\text{A.17})$$

$$p = p^{ss} + \tilde{p} \quad (\text{A.18})$$

$$p_v = p_v^{ss} + \tilde{p}_v \quad (\text{A.19})$$

$$p_L = p_L^{ss} + \tilde{p}_L \quad \text{paul20} \quad (\text{A.20})$$

where, \mathbf{u}^{ss} is the (temporally) constant steady state part of \mathbf{u} , and $\tilde{\mathbf{u}}$ is its (temporally) fluctuating part.

Then equations (A.1), (A.2), (A.3) and (A.13) remain valid with \mathbf{u} replaced by $\tilde{\mathbf{u}}$, p replaced by \tilde{p} , etc. In particular, in the special case $\tilde{p}_v = \tilde{p}_L = 0$, equation (A.13) becomes

$$\nabla \cdot \dot{\tilde{\mathbf{u}}} + \nabla \cdot \dot{\tilde{\mathbf{w}}} + \chi \tilde{p} = 0. \quad \text{paul18} \quad (\text{A.21})$$

Here, $\chi = \chi_v + \chi_L$ is the total microvascular filtration coefficient.

Substituting equation (A.21) into (A.2) and dropping the tildes yields equation (1). Substituting equation (A.1) into (A.3), using equations (A.16-A.20) and dropping the tildes gives equation (2).

Appendix B. One dimensional analytical solution

Under the assumptions outlined in section 2.1.1, we find that the pressure and lateral displacement are both independent of the vertical coordinate, i.e. $p = p(x, t)$ and $u_x = u_x(x, t)$. Further, the lateral normal stress vanishes, i.e. $\sigma_{xx}^t = 0$. Finally, for a step function applied displacement, the vertical displacement is simply $u_y = u_y(y, t) = -u_0 H(t)(y/h)$, where $H(t)$ is the step function. Thus the problem reduces to a 1D problem and Equations (1) and (2) reduce to:

$$\frac{\partial \dot{u}_x}{\partial x} - \kappa \frac{\partial^2 p}{\partial x^2} + \chi p = 0 \quad (B.1)$$

$$\frac{\partial p}{\partial x} - (\lambda + 2\mu) \frac{\partial^2 u_x}{\partial x^2} = 0 \quad (B.2)$$

Integrating Equation (B.2) over x and using Equation (A.1) (note that $\frac{\partial u_y}{\partial y} = -u_0/h$), gives:

$$p - (\lambda + 2\mu) \frac{\partial u_x}{\partial x} = -\lambda \frac{u_0}{h} \quad (B.3)$$

Taking the time derivative of Equation (B.3) and using it in Equation (B.1), yields

$$\dot{p} - \hat{\kappa} \frac{\partial^2 p}{\partial x^2} + \hat{\chi} p = 0 \quad (B.4)$$

Here we have introduced the symbols $\hat{\kappa} = \kappa(\lambda + 2\mu)$ and $\hat{\chi} = \chi(\lambda + 2\mu)$.

Equation (B.4) can then be solved using separation of variables to obtain:

$$p(x, t) = \frac{4\mu u_0}{Lh} \sum_{n=1}^{\infty} \left(\frac{\beta_n}{\alpha_n} \right) \sin(\alpha_n x) e^{-\gamma_n t} \quad (B.5)$$

where $\alpha_n = \frac{n\pi}{L}$, $\beta_n = 1 - (-1)^n$ and $\gamma_n = \alpha_n^2 \hat{\kappa} + \hat{\chi}$. Using Equation (B.3) and the fact that $u_x = 0$ at $x = \frac{L}{2}$, for all time gives:

$$u_x(x, t) = \frac{\lambda u_0 L}{h(\lambda + 2\mu)} \left(x - \frac{L}{2} \right) - \frac{4\mu u_0}{Lh(\lambda + 2\mu)} \sum_{n=1}^{\infty} \frac{\beta_n}{\alpha_n^2} \left(\cos(\alpha_n x) - \cos\left(\frac{n\pi}{2}\right) \right) e^{-\gamma_n t} \quad (B.6)$$

To extend the solution to a case where a ramp function is applied, we take advantage of the fact that a ramp is the integral of the step function. Therefore we integrate Equations (B.5) and (B.6) from $t = 0$ to $t = t_1$. This yields:

$$p(x, t) = \begin{cases} \frac{4a\mu}{Lh} \sum_{n=1}^{\infty} \left(\frac{\beta_n}{\alpha_n} \right) \sin(\alpha_n x) \frac{1 - e^{-\gamma_n t}}{\gamma_n} & , t \leq t_1 \\ \frac{4a\mu}{Lh} \sum_{n=1}^{\infty} \left(\frac{\beta_n}{\alpha_n} \right) \sin(\alpha_n x) \frac{e^{\gamma_n(t_1-t)} - e^{-\gamma_n t}}{\gamma_n} & , t > t_1 \end{cases} \quad (B.7)$$

and

$$u_x(x, t) = \begin{cases} \lambda \hat{a} \left(x - \frac{L}{2} \right) t - \Delta_{1n} & , t \leq t_1 \\ \lambda \hat{a} \left(x - \frac{L}{2} \right) t - \Delta_{2n} & , t > t_1 \end{cases} \quad (B.8)$$

where

$$\Delta_{1n} = \frac{4\mu\hat{a}}{L} \sum_{n=1}^{\infty} \frac{\beta_n}{\alpha_n^2} (\cos(\alpha_n x) - \cos(\frac{n\pi}{2})) \frac{1 - e^{-\gamma_n t}}{\gamma_n} \quad (\text{B.9})$$

$$\Delta_{2n} = \frac{4\mu\hat{a}}{L} \sum_{n=1}^{\infty} \frac{\beta_n}{\alpha_n^2} (\cos(\alpha_n x) - \cos(\frac{n\pi}{2})) \frac{e^{\gamma_n(t_1-t)} - e^{-\gamma_n t}}{\gamma_n} \quad (\text{B.10})$$

and $\hat{a} = \frac{a}{h(\lambda + 2\mu)}$, for an applied displacement given by $u_y = \begin{cases} at & , t \leq t_1 \\ at_1 & , t > t_1 \end{cases}$.

References

- [1] Nightingale K, Palmeri M, Nightingale R and Trahey G 2001 On the feasibility of remote palpation using acoustic radiation force *J. Acoust. Soc. Am.* **110**(1) 625–634
- [2] Nightingale K, Nightingale R, Stutz D and Trahey G 2002 Acoustic radiation force impulse imaging of in vivo vastus medialis muscle under varying isometric load *Ultrason. Imaging* **24**(2) 100–108
- [3] Tanter M, Bercoff J, Sandrin L and Fink M 2002 Ultrafast compound imaging for 2-d motion vector estimation: Application to transient elastography *IEEE Trans. Ultrason. Ferroelectr. Freq. Control* **49**(10) 1363–1374
- [4] Ophir J, Cespedes I, Ponnekanti H, Yazdi Y and Li X 1991 Elastography - A Quantitative Method for Imaging the Elasticity of Biological Tissues *Ultrasonic Imaging* **13** 111–134
- [5] Ophir J, Alam S, Garra B, Kallel F, Konofagou E, Krouskop T and Varghese T 1999 Elastography: ultrasonic estimation and imaging of the elastic properties of tissues *Proceedings of the Institution of Mechanical Engineers Part H-Journal of Engineering in Medicine* **213 (H3)** 203–233
- [6] Bamber J, Barbone P, Bush N, Cosgrove D, Doyley M, Fuechsel F, Meaney P, Miller N, Shiina T and Tranquart F 2002 Progress in Freehand Elastography of the Breast *IEICE Transactions on Information and Systems* **E85D (1)** 5–14
- [7] Muthupillai R, Lomas D J, Rossman P J, Greenleaf J F, Manduca A and Ehman R L 1995 Magnetic Resonance Elastography by Direct Visualization of Propagating Acoustic Strain Waves *Science* **269** 1854–1857
- [8] Kruse S A, Smith J A, Lawrence A J, Dresner M A, Manduca A, Greenleaf J F and Ehman R L 2000 Tissue Characterization Using Magnetic Resonance Elastography: Preliminary Results *Physics in Medicine and Biology* **45** 1579–1590
- [9] Parker K, Gao L, Lerner R and Levinson S 1996 Techniques for elastic imaging: a review *Engineering in Medicine and Biology Magazine, IEEE* **15**(6) 52–59
- [10] Taylor L S, Porter B C, Rubens D J and Parker K J 2000 Three-dimensional Sonoelastography: Principles and Practices *Physics in Medicine and Biology* **45** 1477–1494
- [11] Berry G P, Bamber J C, Armstrong C G, Miller N R and Barbone P E 2006 Towards an acoustic model-based poroelastic imaging method: I. theoretical foundation *Ultrasound in Medicine and Biology* **32**(4) 547–67
- [12] Berry G P, Bamber J C, Armstrong C G, Miller N R and Barbone P E 2006 Towards an acoustic model-based poroelastic imaging method: II. experimental investigation *Ultrasound in Medicine and Biology* **accepted**
- [13] Mow V C, Kuei S C, Lai W M and Armstrong C G 1980 Biphasic creep and stress relaxation of articular cartilage in compression: Theory and experiments *Journal of Biomechanical Engineering* **102** 73–84
- [14] Armstrong C G, Lai W M and Mow V C 1984 An analysis of the unconfined compression of articular cartilage *Journal of Biomechanical Engineering* **106** 165–173
- [15] Biot M A 1941 General theory of three dimensional consolidation *Journal of Applied Physics* **12** 155–164
- [16] Netti P A, Baxter L T, Boucher Y, Skalak R and Jain R K 1997 Macro- and Microscopic Fluid Transport in Living Tissues: Application to Solid Tumors *AIChE Journal of Bioengineering, Food, and Natural Products* **43**(3) 818–834
- [17] Melody A, Swartz M A, Kaipainen A, Netti P A, Brekken C, Boucher Y, Grodzinsky A J and Jain R K 1999 Mechanics of interstitial-lymphatic fluid transport: theoretical foundation and experimental validation *Journal of Biomechanics* **32** 1297–1307

- [18] Sridhar M, J L and Insana M F June 2006 Elasticity imaging of polymeric media *Applied Mechanics Reviews* **submitted**
- [19] Insana M F and Oelse M 2006 in J Suri, R Rangayyan and S Laxminarayan, eds, *Emerging Technologies in Breast Imaging and Mammography* (Valencia CA: American Scientific Publishers) p in press
- [20] Netti P A, Baxter L T, Boucher Y, Skalak R and Jain R K 1995 Time-dependent behavior of interstitial fluid pressure in solid tumors: implications for drug delivery *Cancer Research* **55(22)** 5451–5458
- [21] Sevick E and Jain R 1991 Measurement of capillary filtration coefficient in a solid tumor *Cancer Research* **51(4)** 1352–55
- [22] Sarvazyan A P 2001 in Levy, Bass and Stern, eds, *Handbook of elastic properties of solid, liquid and gases - Vol III: Elastic properties of solids: Biological and organical materials, earth and marine sciences* (New York: Academic) chap 5
- [23] Krouskop T A, Wheeler T M, Kallel F, Garra B and Hall T 1998 Elastic moduli of breast and prostate tissues under compression *Ultrasonic Imaging* **20(4)** 260–274
- [24] Wellman P, Howe R, Dalton E and Kern K 1999 Breast Tissue Stiffness in Compression is Correlated to Histological Diagnosis Tech. rep. Harvard BioRobotics Laboratory, Division of Engineering and Applied Sciences, Harvard University
- [25] Erkamp R Q, Wiggins P, Skovoroda A R, Emelianov S Y and O'Donnell M 98 Measuring the Elastic Modulus of Small Tissue Samples *Ultrasonic Imaging* **20** 17–28
- [26] Spilker R and Maxian T A 1990 A mixed-penalty finite element formulation of the linear biphasic theory for soft tissues *International Journal for Numerical Methods in Engineering* **30** 1063–1082

Figure captions

- Fig. 1** A rectangular homogeneous tissue sample in an unconfined compression test. The sample has dimensions of $L \times h$ and fluid can flow freely across the lateral boundaries ($p = 0$), which are also traction free. The fluid cannot flow across the top and bottom boundaries, which are also shear stress free (slip boundary conditions). $u_y = 0$ at the bottom while a displacement step (or ramp) function is applied at the top.
- Fig. 2** The solution for pressure (Equation (B.7)), at $t = 0.3sec$, $t = 5.4sec$ and $t = 9.9sec$, for $L = 10cm$, $h = 10cm$, $a = \frac{1cm}{0.3sec}$ and $t_1 = 0.3sec$. For the blue line, the poroelastic parameters are chosen such that the fluid exchange between compartments is the dominant phenomenon. These parameters are listed in Table I and correspond to the inclusion in Experiment 1. For the red line, we increase κ 10,000 times and decrease χ 1,000 times.
- Fig. 3** The strain field, ϵ_{xx} , at $t = 5.4 sec$, for both cases shown in Figure 3. In (a), in agreement with the pressure field, we see that the strain is approximately constant along almost the whole sample, indicating that the percolation is negligible outside the very thin boundary layers located at the sample laterals. In (b) we see that the strain varies with x , indicating that percolation is important.
- Fig. 4** Experiment 1: Unconfined Compression. The circular inclusion has 1 cm diameter and the sample has dimensions 10 cm \times 10 cm. The fluid *cannot* flow across the boundaries. The tissue is fixed at the bottom, where $u_x=u_y=0$. The lateral surfaces are traction free. At the top, we simulate the mechanical loading from a compressor of 5 cm width. The displacement of the compressor is modeled by a ramp function such that the prescribed u_y goes from 0 to 1 cm in 0.3 sec, in the region corresponding to $x = 2.5cm$ to $x = 7.5cm$. Below the compressor we prescribe zero shear stress (τ_{yx}).
- Fig. 5** Experiment 2: Confined Compression. The circular inclusion has 1 cm diameter and the sample has dimensions of 10 cm \times 10 cm. The fluid cannot flow across the boundaries and the tissue is fixed at the bottom. The model is completely confined at the top, where u_y goes from 0 to 0.03 cm in 0.3 sec, and is partially confined on the sides from $y = 2.0cm$ to $y = 10cm$, while it is traction free from $y = 0.0cm$ to $y = 2.0cm$. The goal is to reproduce a situation of partial confined test.
- Fig. 6** Experiment 1 Results: Unconfined compression. (a-c) The pressure field (KPa) at $t = 0.3sec$, $t = 5.4sec$, and $t = 10.2sec$, respectively. (d) Initial change of dilatation with time: $\Delta(t = 5.4 sec) - \Delta(t = 0.3 sec)$. (e) Later change of dilatation with time: $\Delta(t = 15.0 sec) - \Delta(t = 10.2 sec)$. (f) Initial change of vertical strain with time: $\epsilon_{yy}(t = 5.4 sec) - \epsilon_{yy}(t = 0.3 sec)$. (g) Later change of vertical strain with time: $\epsilon_{yy}(t = 15.0 sec) - \epsilon_{yy}(t = 10.2 sec)$. Comparing (a) and (b) shows that the inclusion relaxes much faster than the surrounding tissue, due to the higher value of the microvascular filtration coefficient. In (d) we see that during the first five seconds, the inclusion shrinks as it relaxes while the surrounding tissue remains almost unchanged ($\Delta \approx 0$.) In (e) we see that from 10 – 15 sec, the inclusion and surrounding tissue relax similar small amounts.
- Fig. 7** Experiment 2 Results: Confined compression. (a-c) The pressure field (KPa) at $t = 0.3sec$, $t = 6.3sec$, and $t = 13.5sec$, respectively. (d) Initial change

of dilatation with time: $\Delta(t = 6.3 \text{ sec}) - \Delta(t = 0.3 \text{ sec})$. (e) Later change of dilatation with time: $\Delta(t = 31.5 \text{ sec}) - \Delta(t = 13.5 \text{ sec})$. (f) Initial change of vertical strain with time: $\epsilon_{yy}(t = 6.3 \text{ sec}) - \epsilon_{yy}(t = 0.3 \text{ sec})$. (g) Later change of vertical strain with time: $\epsilon_{yy}(t = 31.5 \text{ sec}) - \epsilon_{yy}(t = 13.5 \text{ sec})$. In (a) we see a highly uniform pressure field due to the confined compression boundary conditions. In (d) we see that the initial inclusion shrinkage is about the same as the previous case. In (e) we see that from $t = 13.5 \text{ sec}$ to $t = 31.5 \text{ sec}$ the inclusion swells while the surrounding tissue shrinks. In fact, the inclusion attains its smallest volume at approximately $t = 13.5 \text{ sec}$.

Fig. 8 Experiment 3 Results: Unconfined compression with elevated interstitial permeability. (a-c) The pressure field (KPa) at $t = 0.3 \text{ sec}$, $t = 5.4 \text{ sec}$, and $t = 10.2 \text{ sec}$, respectively. (d) Initial change of dilatation with time: $\Delta(t = 5.4 \text{ sec}) - \Delta(t = 0.3 \text{ sec})$. (e) Later change of dilatation with time: $\Delta(t = 15.0 \text{ sec}) - \Delta(t = 10.2 \text{ sec})$. (f) Initial change of vertical strain with time: $\epsilon_{yy}(t = 5.4 \text{ sec}) - \epsilon_{yy}(t = 0.3 \text{ sec})$. (g) Later change of vertical strain with time: $\epsilon_{yy}(t = 15.0 \text{ sec}) - \epsilon_{yy}(t = 10.2 \text{ sec})$. The dominant effect of increased permeability is to smooth out the fields shown in Figure 6. By comparison to Figure 6, we see that the spatio-temporal patterns of pressure and strain are changed relatively little despite increasing increasing the interstitial permeability by a factor of 100.

Fig. 9 (a) The pressure field (KPa) at $t = 0.3 \text{ sec}$. (b) The pressure field (KPa) at $t = 5.4 \text{ sec}$. (c) The pressure field (KPa) at $t = 10.2 \text{ sec}$. Due to the small interstitial permeability, the effect of the permeable boundary is imperceptible inside the region of interest, being confined to a very thin layer located at the lateral surfaces.

Fig. 10 A portion of soft tissue. Its boundary and volume are represented by Γ and Ω , respectively. Its total volume, Ω , is divided into three different compartments: the interstitial compartment, the hemal vascular compartment and the lymphatic vascular compartment. The interstitial compartment is itself a biphasic solid-fluid mixture, where both fluid and solid phases can move independently of each other.

Tab. 1 Poroelectric parameters used in simulations.

Parameters	Healthy tissue Value	Inclusion Value
$\chi \text{ (Pa}\cdot\text{sec)}^{-1}$	1.89×10^{-8}	5.67×10^{-7}
$\kappa \text{ (m}^2\text{/Pa}\cdot\text{sec)}$	6.4×10^{-15}	3.1×10^{-14}
$\lambda \text{ (KPa)}$	539	517
$\mu \text{ (KPa)}$	11	33

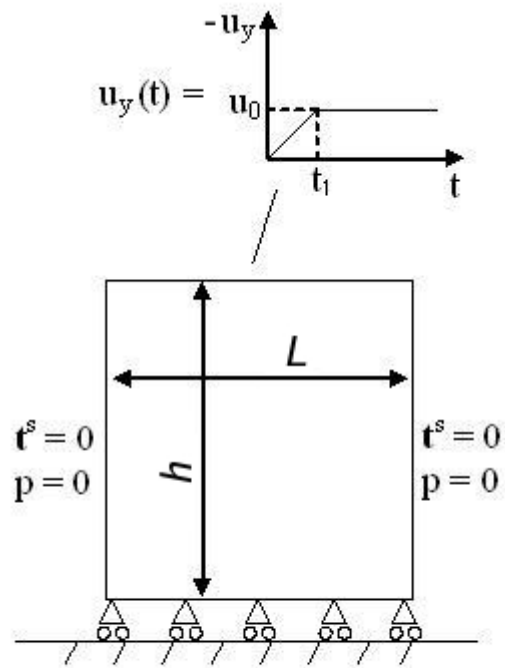


Figure 1

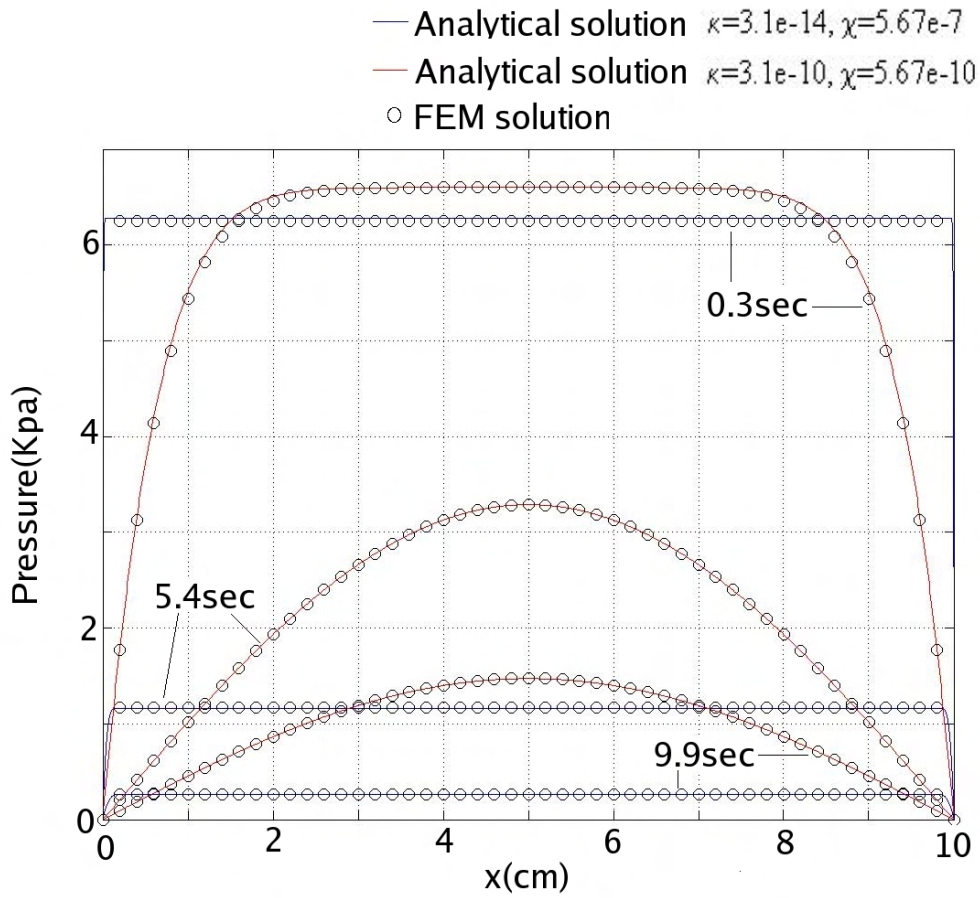


Figure 2

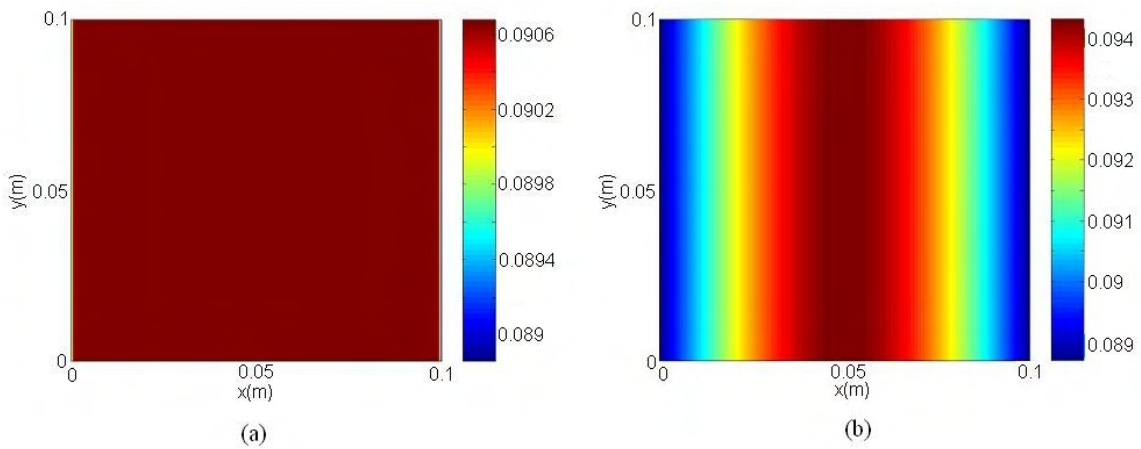


Figure 3

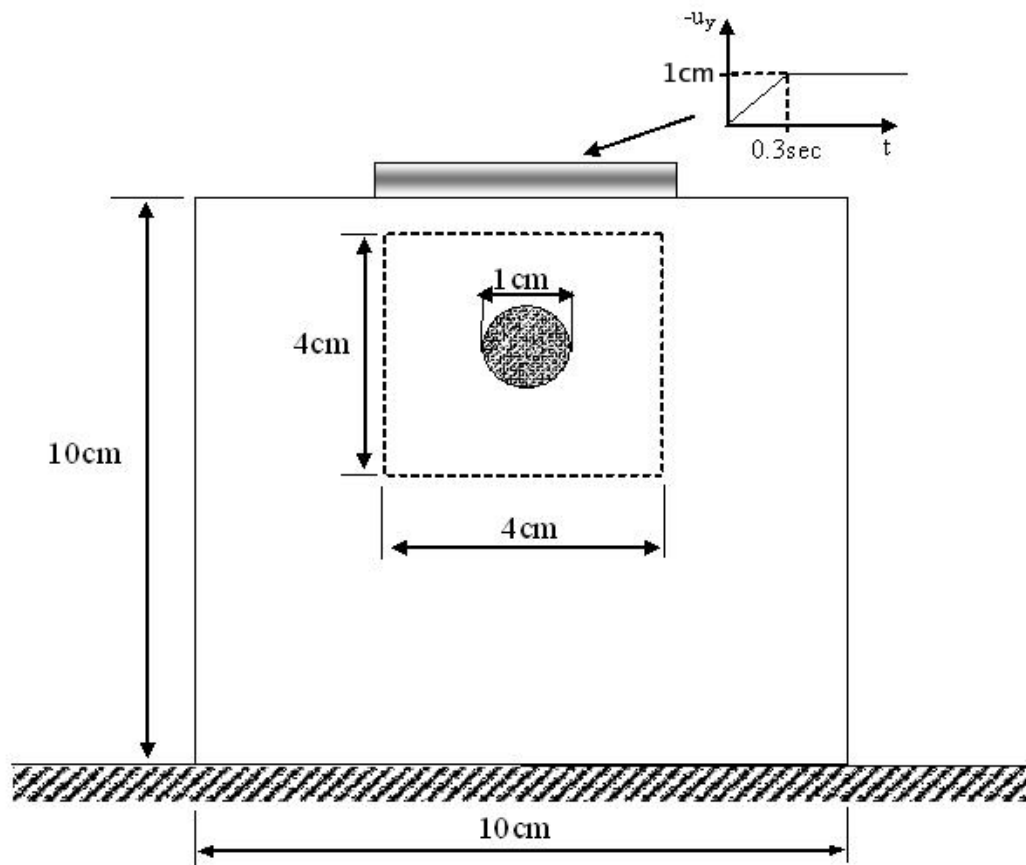


Figure 4

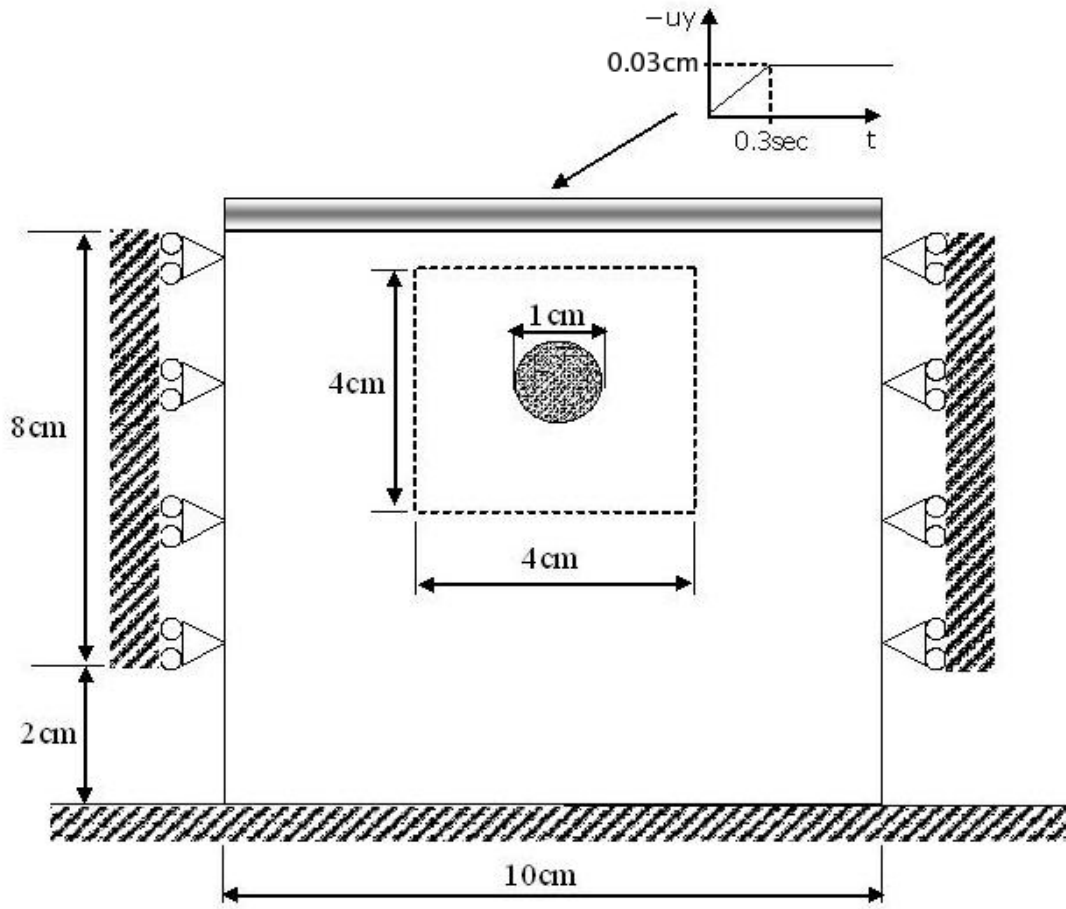


Figure 5

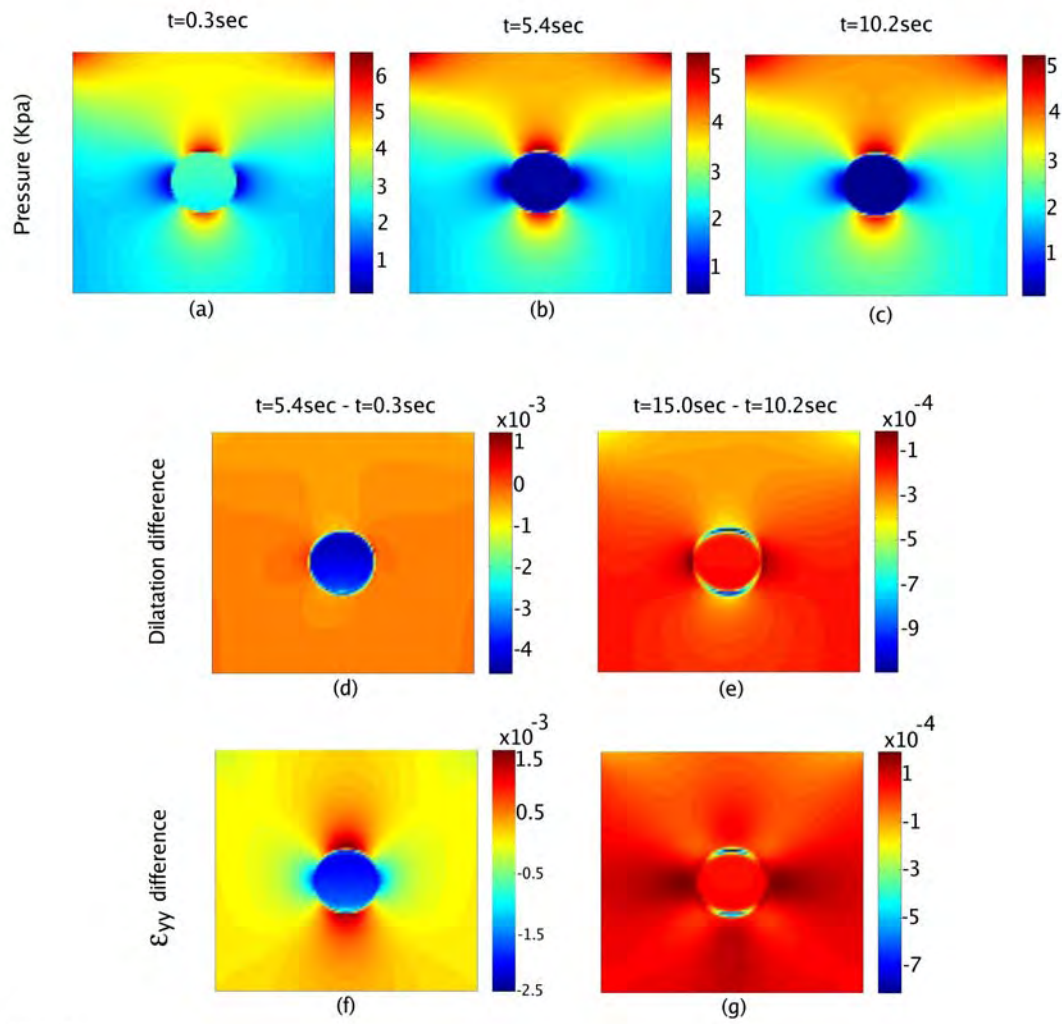


Figure 6

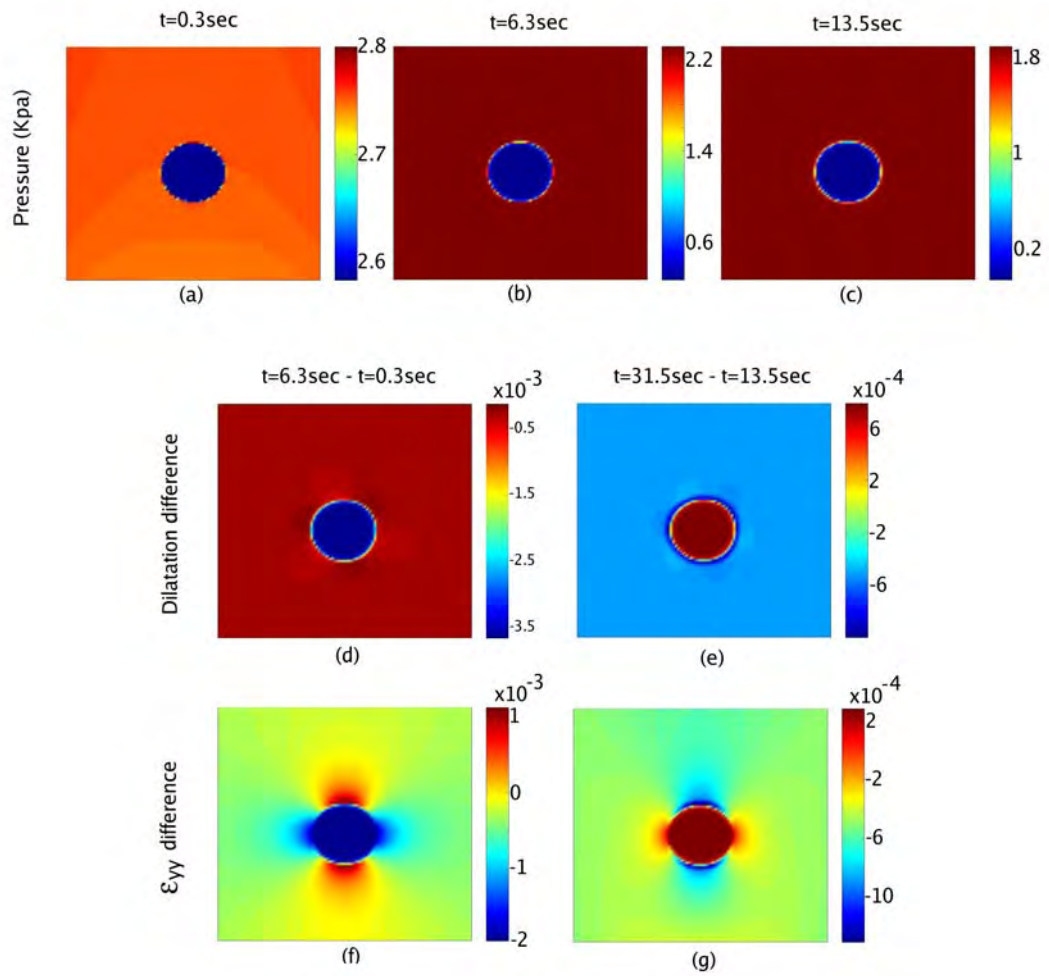


Figure 7

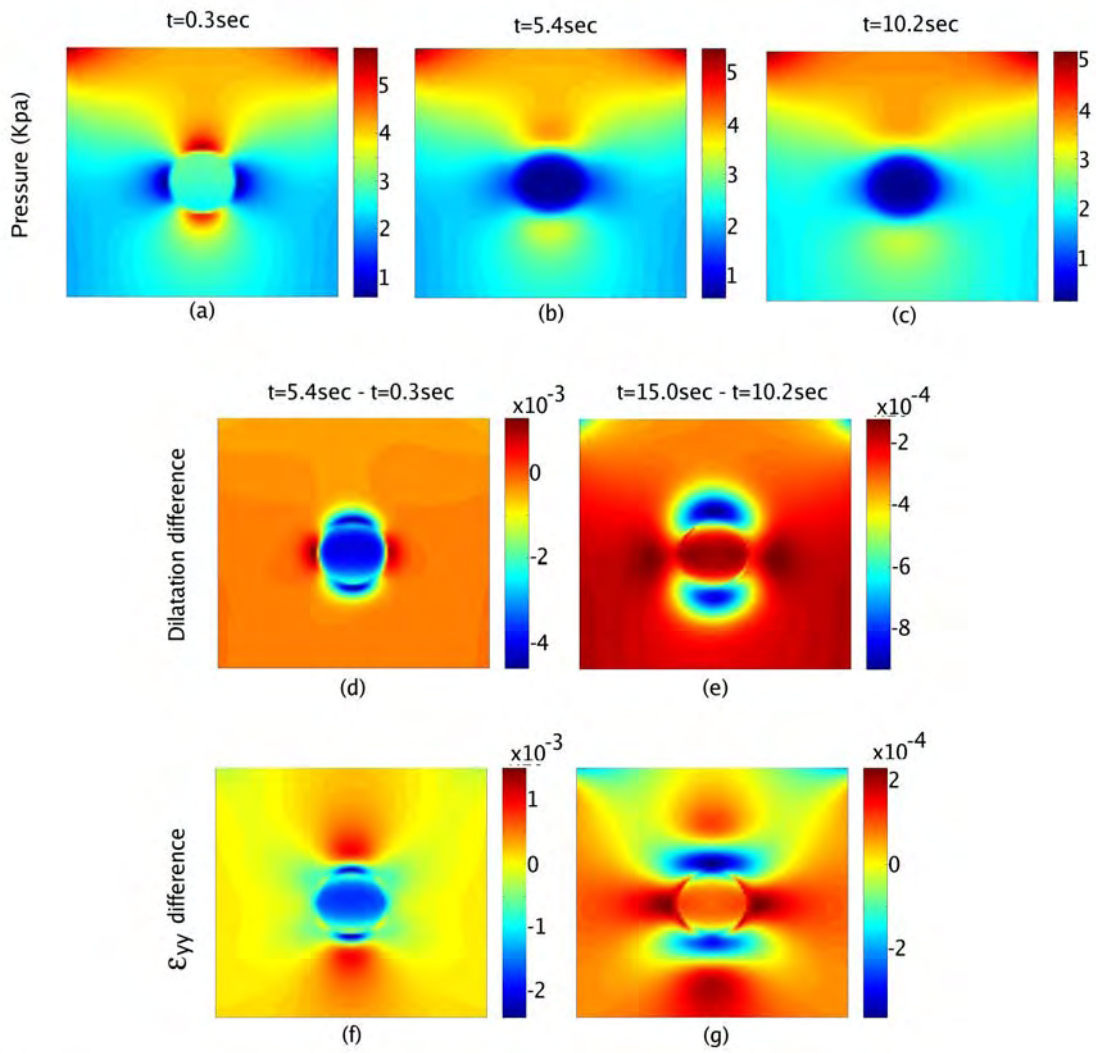


Figure 8

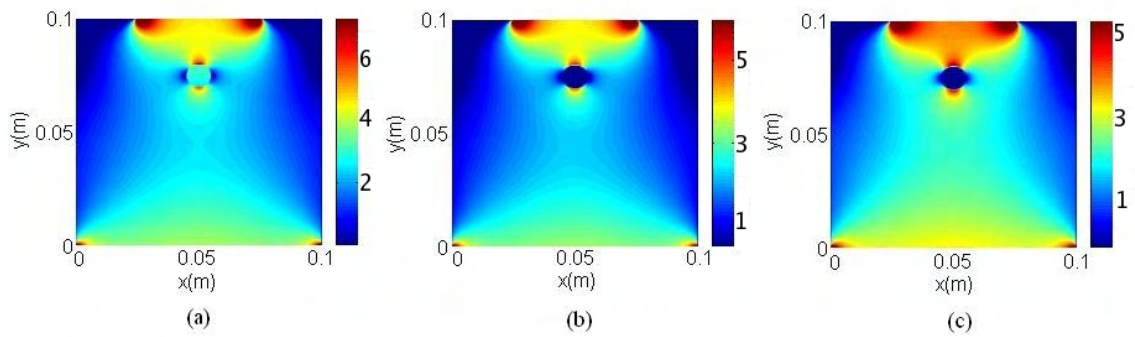


Figure 9

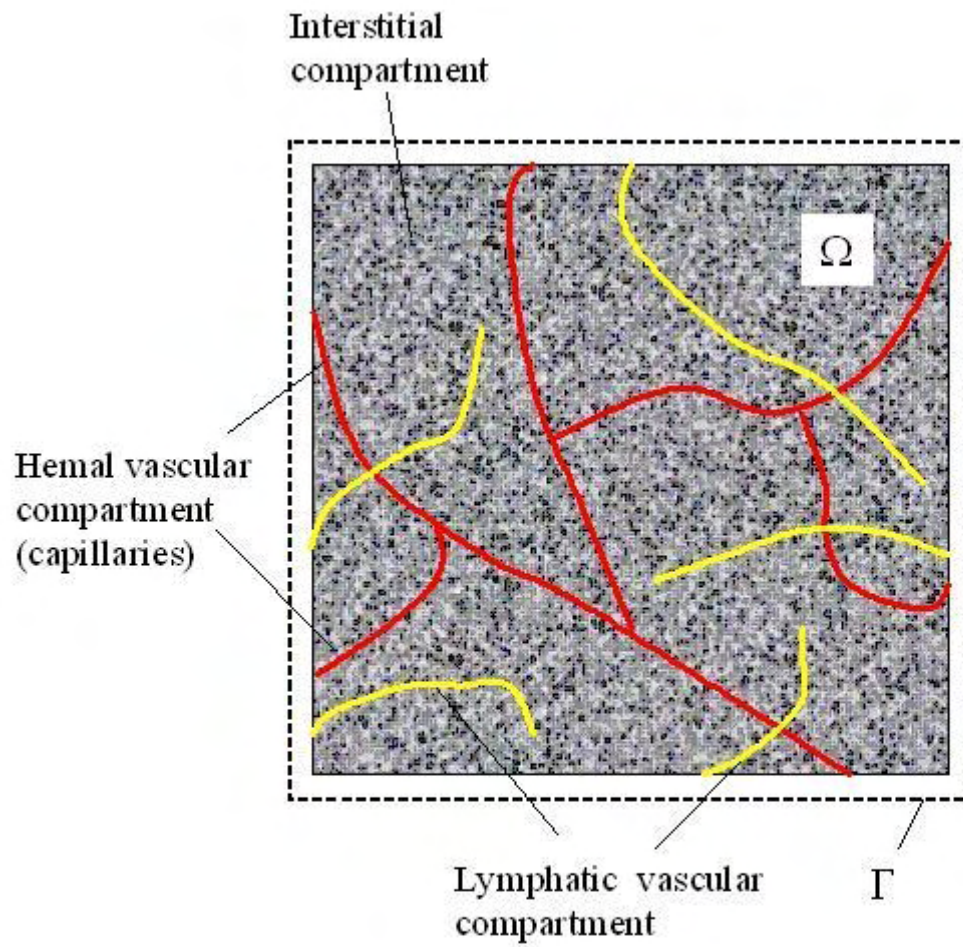


Figure 10